

GEMINI/GNIRS OBSERVATIONS OF THE CENTRAL SUPERMASSIVE BLACK HOLE IN CENTAURUS A

JULIA D. SILGE AND KARL GEBHARDT

Department of Astronomy, University of Texas at Austin, 1 University Station C1400, Austin, TX 78712
dorothea@astro.as.utexas.edu, gebhardt@astro.as.utexas.edu

MARCEL BERGMANN

NOAO Gemini Science Center (Chile), P.O. Box 26732, Tucson, AZ 85726
mbergmann@noao.edu

DOUGLAS RICHSTONE

Department of Astronomy, University of Michigan at Ann Arbor, 830 Dennison, 501 East University Avenue, Ann Arbor, MI 48109
dor@astro.lsa.umich.edu
Draft version August 8, 2018

ABSTRACT

The infrared spectrograph GNIRS on Gemini South unlocks new possibilities to study the central black holes in dusty galaxies that have been inaccessible to previous black hole studies. We exploit good near-infrared seeing to measure the central black hole (BH) of Centaurus A (NGC 5128). We measure the stellar kinematics of NGC 5128 using the region around the CO bandheads at $2.3 \mu\text{m}$ and determine the black hole mass using orbit-based models. Black holes are believed to be essential components of galaxies, and their evolutionary states appear to be closely linked to those of their hosts. Our current knowledge does not go much beyond this; galaxies such as NGC 5128 (an AGN and recent merger) can further develop this knowledge. However, NGC 5128 and galaxies like it contain large amounts of dust which hamper optical spectroscopy, making near-infrared measurements an attractive alternative. We find a BH mass of $2.4^{+0.3}_{-0.2} \times 10^8 M_{\odot}$ for an edge-on model, $1.8^{+0.4}_{-0.4} \times 10^8 M_{\odot}$ for a model with inclination of 45° , and $1.5^{+0.3}_{-0.2} \times 10^8 M_{\odot}$ for a model with inclination of 20° . We adopt the value for the edge-on model, which has significantly lower χ^2 . These estimates are consistent with a previous gas dynamical estimate and are five to ten times higher than that predicted by the correlation between BH mass and velocity dispersion. If NGC 5128 will eventually follow the trend for quiescent galaxies, this result suggests that its BH assembled first before its host component. NGC 5128 thus provides an important example for our knowledge of central black holes; this technique can be applied to other such galaxies to further explore this question.

Subject headings: galaxies: active — galaxies: individual (NGC 5128) — galaxies: kinematics and dynamics

1. INTRODUCTION

NGC 5128 (Centaurus A) is an important object for our understanding of central black holes, galaxy mergers, AGN activity, and the relationships among these components of galaxy evolution. However, the very characteristics which make this galaxy so interesting have also been serious roadblocks to more detailed knowledge. NGC 5128 contains large amounts of dust which hamper optical spectroscopy, especially in the central regions which are so critical for accurately measuring the black hole (BH) mass. We measure the stellar kinematics of NGC 5128 using new data from the Gemini Near Infrared Spectrograph (GNIRS) at Gemini South; we utilize the region around the CO bandheads at $2.3 \mu\text{m}$. This observational treatment opens up a new avenue for black hole research as it allows us to probe the most interesting galaxies; NGC 5128 is the prime example.

NGC 5128 is our nearest neighbor galaxy harboring a powerful central AGN. It is a massive elliptical galaxy which hosts a strong, variable X-ray/radio source and a massive, complex disk composed of dust, gas, and young stars. The unusual morphology of NGC 5128 was first ascribed to a significant and recent merger event by Baade & Minkowski (1954). This merger hypothesis is well-supported by the existence of optical and HI shells at large radii and the polar

orientation of the disk of dust and gas along the photometric minor axis of the galaxy (Malin, Quinn, & Graham 1983; Quillen, Graham, & Frogel 1993; Israel 1998). The recent merger activity and central AGN are likely associated with each other, and make NGC 5128 an interesting case for BH studies. Its notable proximity makes it an attractive target, as spatial resolution on the sky translates to small linear scales in the galaxy itself.

The correlation (Gebhardt et al. 2000a,b; Ferrarese & Merritt 2000) in bulge galaxies between central black hole mass (a local property) and velocity dispersion (a global property) sheds light on the formation and evolutionary histories of both the black hole and its host. Many theories (Silk & Rees 1998; Haehnelt & Kauffmann 2000; Ostriker 2000; King 2003) predict such a correlation, and with the many models that have been presented to date, none have been excluded. One of the best ways to determine the underlying physics is to study those galaxies that have an active nucleus, i.e. have a central BH which is actively accreting material, such as NGC 5128. If these galaxies lie in a different regime in correlation studies, we can begin to understand the governing processes and roles of bulge and BH growth. Gebhardt et al. (2000b) use reverberation mapping estimates of the BH masses of AGN galaxies and

find the same correlation as for quiescent galaxies. NGC 5128 is much closer than any of these galaxies and thus we can make a more precise measurement of the BH using stellar kinematics, the technique used for normal local galaxies. Also, NGC 5128's recent merger history holds implications for the BH- σ correlation; we can extend the parameter space within which we know how galaxies behave in this correlation.

Although galaxies with active nuclei have been a large motivation in the search for BHs, it is difficult to make a direct dynamical mass determination for the BHs which we understand to power these AGNs. The nuclei of many AGN galaxies are heavily obscured by dust, and NGC 5128 is no exception. At optical wavelengths, the central nucleus is nearly invisible, veiled by the rich dust lane. Such dust obscuration hampers kinematic measurements made using optical data; the central BH of a galaxy like NGC 5128 cannot be measured using optical data. Moving to the near-infrared allows us to minimize these problems. Near-IR wavelengths are long enough to minimize dust extinction. Also, galaxy light in this spectral regime is dominated by the older, redder stellar population and is less affected by recent star formation. Kinematics in this spectral regime should be the best measure of the underlying stellar potential of the galaxy. As infrared instrumentation (such as GNIRS on Gemini South used in this paper) becomes more available and efficient, this region is becoming an important tool in the study of galaxies (Silge & Gebhardt 2003).

With such a motivation, Marconi et al. (2001) provide an estimate of the BH in NGC 5128 using *J*-band and *K*-band gas dynamical measurements. They find a black hole mass of $2 \times 10^8 M_{\odot}$. Given a velocity dispersion for NGC 5128 of $\sim 150 \text{ km s}^{-1}$, we would expect a BH mass around $3 \times 10^7 M_{\odot}$ from the BH- σ correlation. If this BH mass is correct, NGC 5128 has the largest offset ever measured from the BH- σ correlation (currently measured for over forty galaxies). This is an important point. One issue is the difficulty of interpreting gas dynamics. Sarzi et al. (2002) has shown that without a well-ordered gas disk it may be impossible to determine the enclosed mass from such observations. Marconi et al. (2001) claim they see no evidence for strong nongravitational motions, but there are few galaxies with reliable enclosed masses from both gas and stellar kinematics so it is difficult to know how to interpret these results.

Thus, NGC 5128 is important because it has recently undergone a merger, it contains a rich gas disk, its apparently large BH is actively accreting material, and it is on our doorstep. In this paper, we report the BH mass measured from near-infrared stellar kinematics and its offset relative to other galaxies. This data can help us refine our knowledge of how galaxies grow both their bulge and BH. Section 2 presents the data, Section 3 describes the dynamical modeling procedure, Section 4 presents the results for the BH mass for NGC 5128, and Section 5 discusses the implications of these results.

The distance to NGC 5128 is a matter of some debate. Israel (1998) compiles and summarizes results from globular cluster and planetary nebulae counts, globular cluster surface brightness fluctuations, and *HST* observations of halo red giant branch stars; he finds good agreement between these sources with a distance of $D = 3.4 \pm 0.15 \text{ Mpc}$. More recently, the *I*-band surface brightness fluctuation study of the galaxy itself by Tonry et al. (2001) found $D = 4.2 \pm 0.3 \text{ Mpc}$. Rejkuba (2004) measures the Mira period-luminosity relation and the luminosity of the tip of the red giant branch to find

$D = 3.84 \pm 0.35 \text{ Mpc}$. The BH measurement of Marconi et al. (2001) described above assumes $D = 3.5 \text{ Mpc}$; we also use this assumption. At this distance, $1''$ on the sky corresponds to 17 pc .

2. DATA

2.1. Surface Brightness Profile

To measure the BH mass, we need both photometric measurements and kinematic measurements with sufficient spatial resolution and radial extent. We combine *HST* and 2MASS imaging of NGC 5128 to satisfy these needs. *K*-band *HST* observations of NGC 5128 were obtained by Schreier et al. (1998). The nuclear region of NGC 5128 was observed on 11 August 1997 in the F222M filter with an exposure time of 1280 seconds. Schreier et al. (1998) report the azimuthally averaged surface brightness out to a radius of $\sim 10''$. Within $0.65''$, the surface brightness profile of NGC 5128 is dominated by emission from a strong unresolved source, the central AGN. We do not include this light in our dynamical modeling because it does not reflect the stellar density distribution. We extrapolate to radii smaller than $0.65''$ using the *HST* data outside this radius. The logarithm of the surface brightness outside $0.65''$ is nearly linear with $r^{1/4}$, so we extrapolate this $r^{1/4}$ profile inward to our innermost kinematic point. The dynamical modeling is not strongly dependent on this extrapolation because the amount of light (and thus enclosed mass) involved at these small radii is not large and does not have a significant impact on the gravitational potential.

For photometry at larger radii, we utilize the 2MASS Large Galaxy Atlas (LGA) (Jarrett et al. 2003). These authors construct large mosaics for each of the 100 largest galaxies as seen in the near-infrared. Jarrett et al. (2003) join 2MASS scans and iteratively remove the sky background, resulting in carefully constructed, well-calibrated images of these galaxies. We use the *K*-band image of NGC 5128, the tenth largest galaxy in the atlas.

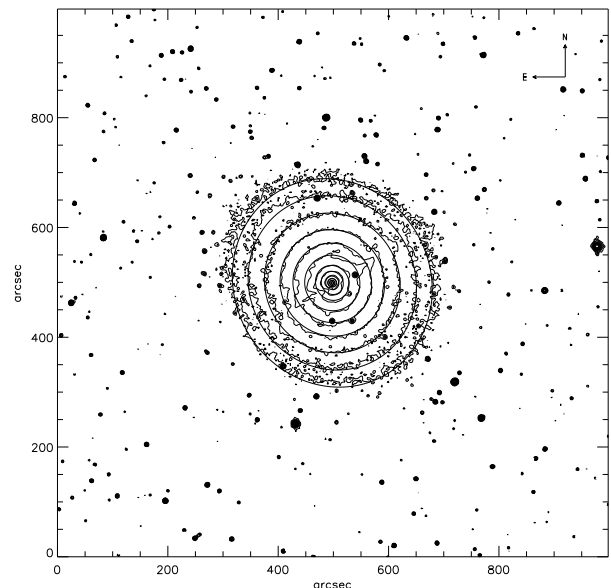


FIG. 1.— Contour map of the 2MASS LGA *K*-band image of NGC 5128. Overlaid are the contours of the MGE best-fitting model; this model's profiles are shown in Figure 2. The contours are logarithmically spaced but arbitrary.

We use the multi-Gaussian expansion (MGE) method of

Cappellari (2002) to fit the surface brightness profile to the 2MASS image. The MGE method is a simple parametrization with an analytic deprojection which is flexible enough to model realistic multicomponent objects. This method uses a series expansion of two-dimensional Gaussian functions to represent galaxy images. Figure 1 shows the result of MGE fitting for NGC 5128; this figure shows a contour map of the 2MASS LGA K -band image with the contours of the best-fitting MGE model superimposed. This model was constructed to have constant position angle with radius; allowing the position angle to vary does not improve the fit. The position angle was fixed at 38 degrees east of north. The best-fit model uses six two-dimensional Gaussian functions to represent the surface brightness of NGC 5128. The dust lane of NGC 5128 is visible even in this K -band image, emphasizing the high level of dust obscuration in this galaxy. The dust lane does not significantly hamper the MGE fitting or the kinematic observations below, however. Figure 2 illustrates this; the left panels show the comparison between the 2MASS photometry and the best-fitting MGE model while the right panels show the radial variation of the relative error along the profiles.

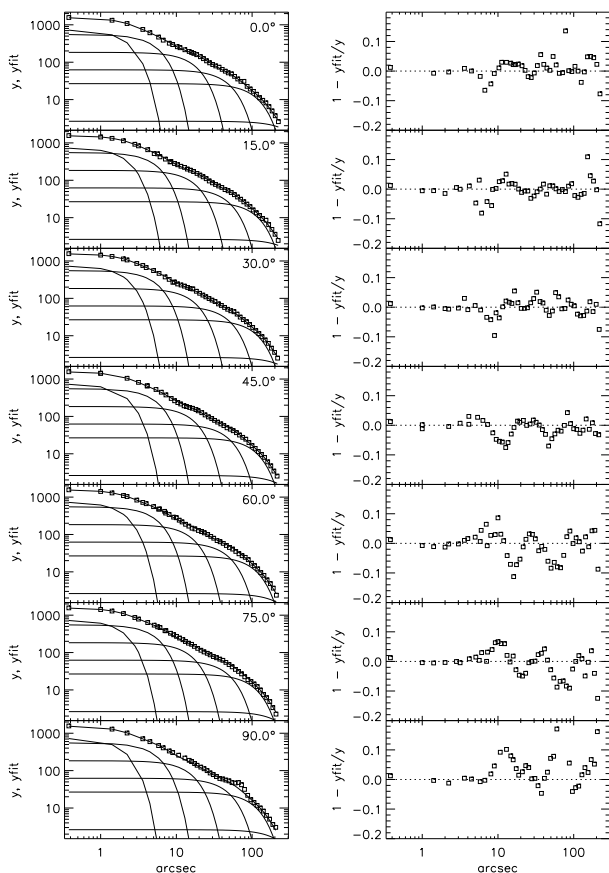


FIG. 2.— Left panels: comparison between the 2MASS LGA K -band photometry of NGC 5128 (open squares) and the ($N=6$) Gaussian MGE best-fitting model (solid line). The individual Gaussian components are also shown. The angles noted in the upper right hand corner of each panel are measured relative to the photometric major axis. Right panels: radial variation of the relative error along the profiles.

The dynamical modeling we use to constrain the BH mass assumes axisymmetry. Evidence exists that NGC 5128 is

moderately triaxial (Israel 1998) but the photometric data suggest that it can be well-represented for our purposes as a spheroid of constant ellipticity. The model with constant position angle fits the surface brightness well, and figure 3 shows that the ellipticity of the galaxy is small and does not change drastically. This figure presents the ellipticity of the MGE best-fitting model as a function of radius; the ellipticity is never much higher than 0.1. Thus, we can represent NGC 5128 in our modeling as a spheroid with constant projected ellipticity of 0.05. Figure 4 presents the final surface brightness profile along the major axis which we use in our dynamical modeling. The dashed line is the profile from the MGE best-fitting model of the 2MASS LGA image and the solid line is the HST profile of Schreier et al. (1998). The HST data have been adjusted to match the 2MASS data between 2 and $10''$; there is good agreement in the shape of the two profiles. The arrow indicates the radius of transition between domination by the AGN and domination by the stellar density distribution; the profile within this radius has been extrapolated from the HST data outside this radius.

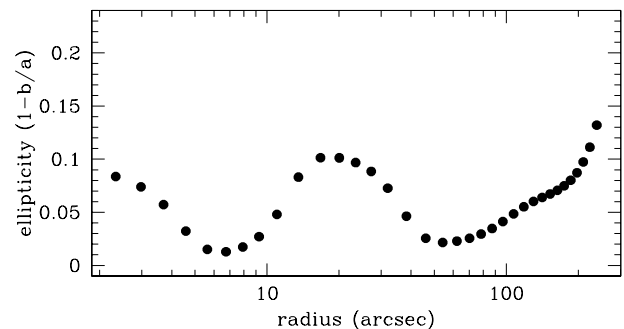


FIG. 3.— K -band ellipticity as a function of radius along the major axis for NGC 5128.

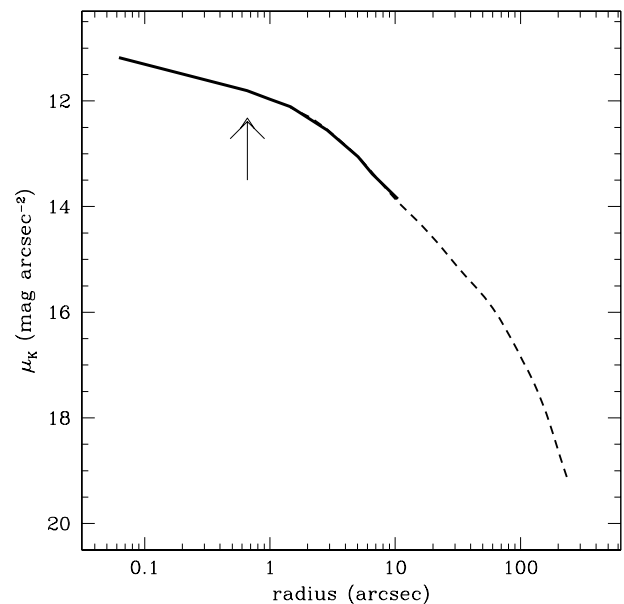


FIG. 4.— K -band surface brightness for NGC 5128. The dashed line is from the MGE fitting of the 2MASS LGA image and the solid line is from the HST data of Schreier et al. (1998). The HST data have been adjusted to match the 2MASS data between 2 and $10''$. The arrow indicates the radius at which light from the AGN dominates; the profile within this radius has been extrapolated from the HST data outside this radius.

NGC 5128 is so enshrouded in dust that it is reasonable to examine how affected observations are by dust even in the K -band. Marconi et al. (2000) report *HST* observations of the nucleus of NGC 5128 in V , I , and H , and K . They assume no color gradients between any of these bands and derive the implied reddening for each band. They report a dereddened K -band surface brightness profile. The shape of this profile is very close to the observed profile, showing deviation only within $\sim 1''$. The dereddened profile is still nearly linear with $r^{1/4}$ so we take the same approach and extend the profile inward into the region dominated by the AGN light, then compare the mass implied by the two profiles. Using the M/L_K ratio implied by the velocity dispersion profile described in Section 2 (and in agreement with the dynamical modeling of Sections 3 and 4), the enclosed stellar mass at $1''$ is $2 \times 10^7 M_\odot$ for the original profile and $3 \times 10^7 M_\odot$ for the dereddened profile. This difference of $1 \times 10^7 M_\odot$ is a small fraction of the BH mass we measure, and thus will not have a significant effect. We ran a small suite of dynamical models using the dereddened profile and found that this is indeed the case; there is no difference in our results. Similarly, this applies to the extrapolation of the stellar light into the region dominated by emission from the AGN. The difference in implied enclosed mass for different extrapolations is even smaller than for the original and dereddened profiles and the results of our modeling are not dependent on changes in this extrapolation.

2.2. Kinematic Observations

NGC 5128 was observed on 2004 March 8 and June 15 as part of system verification for the Gemini Near-Infrared Spectrograph (GNIRS) on Gemini South, using Gemini program identification number GS-2004A-SV-8. GNIRS has a 1024×1024 Aladdin III InSb detector array with a spatial scale of $0''.15 \text{ pixel}^{-1}$. We utilize the long-slit, short-camera mode of GNIRS which can obtain the spectrum of the K -band atmospheric window ($1.9 \mu\text{m}$ to $2.5 \mu\text{m}$) in one exposure. Using a 32 l/mm grating and $0.3'' \times 99''$ slit, we obtained spectral resolution of 1600, measured from calibration lamps lines and night sky lines. With this resolution, we can measure velocity dispersions down to 80 km s^{-1} , much smaller than the dispersion of NGC 5128.

We utilize the K -band CO absorption bandheads from evolved red stars to measure the stellar kinematics of NGC 5128. The $(2-0)^{12}\text{CO}$ absorption bandhead at $2.293 \mu\text{m}$ is the first of a series of many bandheads which stretch out redward. These features are in a dark part of the infrared sky spectrum and are intrinsically sharp and deep, making this region very sensitive to stellar motions (Lester & Gaffney 1994). They are the strongest absorption features in galactic spectra between $1-3 \mu\text{m}$; this region is optimal for studying stellar kinematics because wavelengths are long enough to minimize extinction from dust but short enough to avoid emission from hot dust (Gaffney et al. 1995). Silge & Gebhardt (2003) present a detailed calibration of stellar kinematics measured using the first CO bandhead.

The first observation was made with the slit oriented perpendicular to the inner dust ring (along the major axis at large radii), centered on the bright AGN. The second observation was made with the slit oriented parallel to the dust lane but offset from the center by $0.85''$. Individual exposures were 120 seconds; between exposures on the object, sky exposures of 120 seconds were taken $\sim 200''$ to the southeast. NGC 5128 is very large on the sky and large telescope offsets are required to obtain good sky subtraction. The total on-source

integration time was 2160 seconds for the slit position perpendicular to the dust lane and 1680 seconds for the slit position parallel to the dust lane. We measured the seeing from images of telluric calibration stars and the central unresolved AGN. The seeing during the first observation was $0''.45$; during the second it was $0''.6$.

To remove the shape of the telluric absorption spectrum from our observations, we observed an A0V star (HD107422). A dwarfs have nearly featureless spectra in this region (Wallace & Hinkle 1997); we require a good measure of telluric absorption because we are interested in the detailed shape of the galaxy spectrum. Silge & Gebhardt (2003) present more details on this point. The A0V observations were made by dithering the telescope $10''$ across the slit to measure the sky at the same slit position in alternating exposures.

Wavelength calibration for both galaxy and star observations was carried out using the arc lamps of the Facility Calibration Unit for Gemini South. Guiding was provided by the peripheral wavefront sensor assigned to a star outside the science field for the galaxy or telluric standard. During the off-source sky exposures for the galaxy observations, the guiding was paused and we relied on the telescope tracking because of the difficulty presented by the large offset; this sky subtraction procedure worked well. No attempt is made to flux calibrate the spectra since we are only concerned with the kinematic analysis.

2.3. Data Reduction

Data reduction proceeds similarly to that described in Silge & Gebhardt (2003). We rectify the images in the spectral direction using the arc lamp lines and subtract each sky exposure from its associated object exposure to remove the sky background. The subtracted images are then shifted in the spatial direction so that the center of the galaxy in each image is aligned; we calculate the biweight (Beers et al. 1990) of all the processed images to make one image for the galaxy. The one-dimensional spectra are then extracted from the two-dimensional image in nearly logarithmically spaced spatial bins. The stellar spectra are reduced in a similar manner but extracted in a single aperture. We then remove the telluric absorption spectrum from the galaxy spectra by dividing by a “flat” spectrum, obtained from the A0V. We obtain good results for this spectral flattening compared to our experience with other instruments and sites.

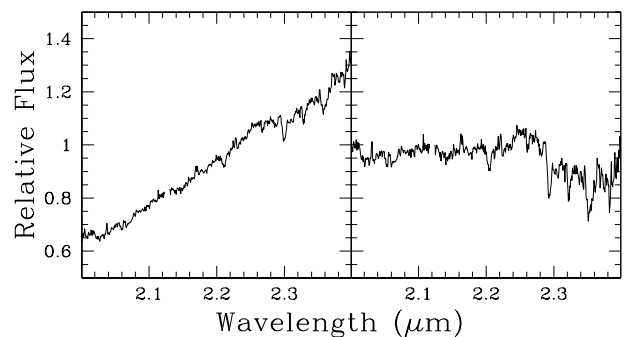


FIG. 5.— Spectrum for one spatial bin $0''.45$ from the galaxy center. The left panel shows the spectrum dominated by the AGN emission; the right panel shows the spectrum after this AGN continuum shape has been removed.

The second observation was taken with the slit offset from the center of the galaxy but the first observation was well-

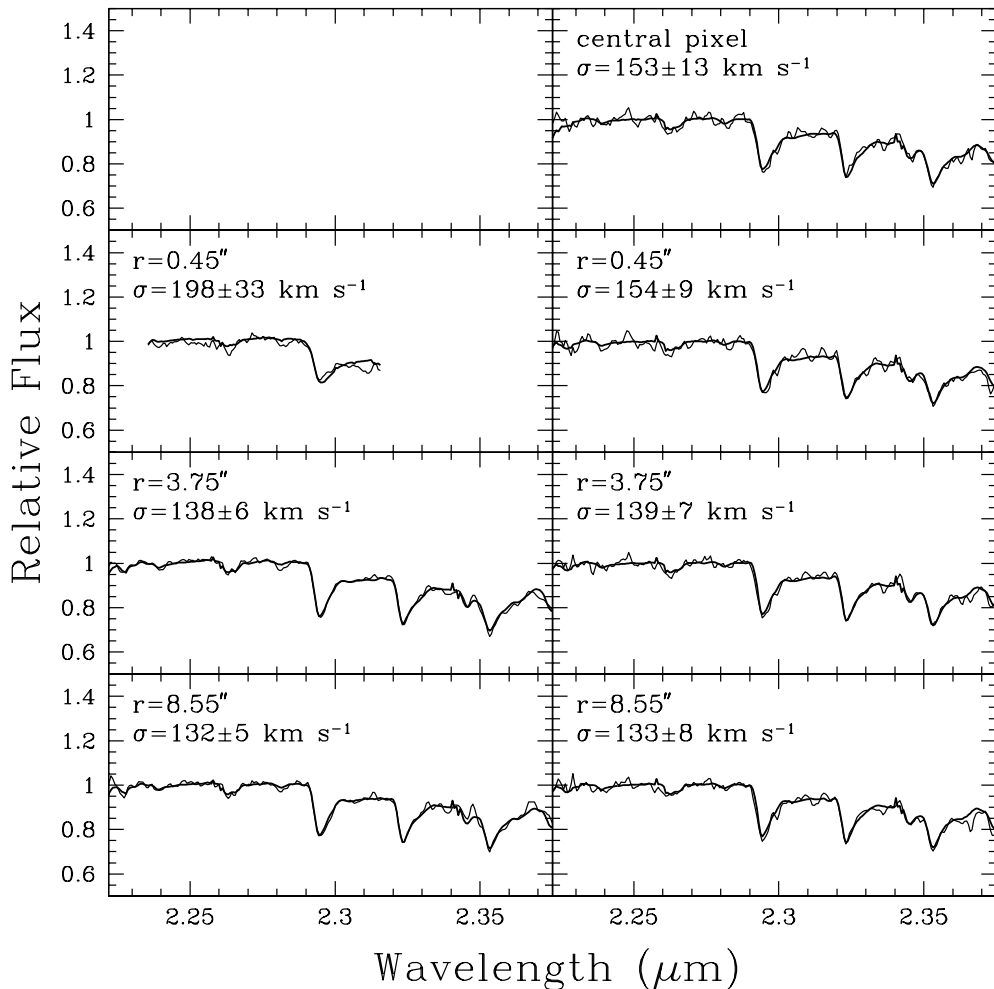


FIG. 6.— Rest-frame spectra for seven example spatial bins (noisy line) and for the template stellar spectrum convolved with the derived LOSVD for that bin (smooth line). The derived second moment of the LOSVD and its 68% uncertainty is reported for each of these bins. The left panels show data from the axis perpendicular to the dust disk; the right panels show data from the axis parallel to the dust disk but offset from the center.

centered on the central nucleus. The spectra in the central spatial bins from this observation are dominated by emission from the central AGN; the CO bandheads are filled in by this emission. We worked to recover some of this information by removing the AGN emission. The equivalent width of the $(2-0)^{12}\text{CO}$ bandhead is largely constant with radius in this galaxy for regions outside the AGN, so we measure the AGN contribution by its dilution of the equivalent width. After this process, we are able to use data within $0''.3$ of the center in the kinematic fitting. Spectra out to $1''$ exhibit changes in equivalent width which require removal of AGN light. Figure 5 illustrates the results of this step for one bin $0''.45$ from the center. The left panel shows the spectrum before removal of the AGN emission and the right panel shows the spectrum after this process, ready for its kinematic fitting.

2.4. Extracting the Velocity Distribution

Once we have the spectrum in each spatial bin, we extract the kinematic information. A galaxy spectrum is the convolution of the line-of-sight velocity distribution (LOSVD) with an average stellar spectrum; to obtain this internal kinematic information, we use the fitting technique of Gebhardt et al.

(2000c), deconvolving the spectrum directly in pixel space using a maximum penalized likelihood estimate to obtain a nonparametric LOSVD. An initial velocity profile is chosen and this profile is convolved with a stellar template spectrum. The residuals to the galaxy spectrum are calculated and the velocity profile is changed to minimize the residuals and provide the closest match to the observed galaxy spectrum.

The choice of template star is important for kinematic fitting using the CO bandheads; this feature is sensitive to template mismatch (Silge & Gebhardt 2003). Thus, we give the fitting program a variety of template stellar spectra and simultaneously fit for the velocity profile and the stellar template weights. As a result, our fitting procedure provides both the LOSVD and stellar population information. We use the near-IR stellar spectral atlas of Wallace & Hinkle (1997) as our templates, choosing eight stars with $(2-0)^{12}\text{CO}$ equivalent widths ranging from less than 5 \AA to over 20 \AA . These spectra have a somewhat higher spectral resolution than ours, so before using them as stellar templates we have carefully convolved them to our spectral resolution using a Gaussian distribution with $\sigma = 5.37 \text{ \AA}$. The best fit almost always gives most

of the weight to a few of the template stars. Figure 6 shows the results for some example spatial bins for NGC 5128. The noisy line is the observed spectrum and the smooth line is the template stellar spectrum convolved with the derived LOSVD. Each frame in figure 6 shows the spectrum in one spatial bin on one side of the galaxy; in the actual fitting we fit both sides of the galaxy simultaneously with the LOSVD flipped around the $v = 0$ axis for the opposite side. For the spatial bins where we removed the AGN emission, we were not able to use the same wavelength region for the fitting. The AGN removal worked best over smaller wavelength regions; in the innermost few bins we fit only the first bandhead while in intermediate bins we fit the first two. From $1''$ outward, we used the full region shown in figure 6.

We determine the uncertainties for the LOSVDs using the Monte Carlo bootstrap approach of Gebhardt et al. (2000c). The initial fit to the observed galaxy spectrum is used to generate 100 simulated spectra with noise chosen to match that of the observed spectrum. These 100 synthetic galaxy spectra are then deconvolved to determine their LOSVDs in the same way the original observed spectrum is deconvolved. These LOSVDs provide a distribution of values for each velocity bin which allows us to estimate the uncertainty and examine any bias in the moments of the LOSVD. The median of the distribution determines any potential bias from the initial fit, and the spread of the distribution determines the uncertainty. In order to generate the 68% confidence bands, we choose the 16% to 84% values from the 100 realizations.

Most LOSVD fitting techniques make some assumption about the shape of the LOSVD, i.e. it is Gaussian or a Gauss-Hermite polynomial. Our technique obtains a nonparametric LOSVD; no a priori assumptions about the shape of the LOSVD are made except that it is nonnegative in all bins and subject to some smoothness constraint. We are able to exploit the full LOSVDs in the dynamical modeling below. We plot the parameterization of the LOSVDs by Gauss-Hermite moments in figure 7 and present them in table 1. The velocity dispersion is very close to 135 km s^{-1} on both axes for most of the radius range ($\sim 2''$ to $\sim 40''$). The luminosity-weighted σ_* using an aperture of $60''$ along the slit parallel to the dust disk is $138 \pm 10 \text{ km s}^{-1}$. The axis perpendicular to the dust lane (which was centered on the galaxy nucleus) shows a steep rise in both σ and h_4 (which indicates a triangular distortion from a Gaussian shape, i.e. strong high velocity wings on the LOSVD) within the central arcsecond. We detect rotation along both axes, the photometric major axis and the axis parallel to the dust disk in the center, as have other authors including Peng, Ford, & Freeman (2004) and Hui, Ford, Freeman, & Dopita (1995). This is not strictly consistent with an axisymmetric model, as we discuss later.

These Gemini observations go out to $\sim 40''$, but this is only about halfway to the half-light radius. According to Jarrett et al. (2003), the K -band half-light radius is $r_{eff} = 82.6''$. Limited spatial extent can significantly reduce the precision to which one can measure the BH mass (Richstone et al. 2004) so we include kinematic data at larger radii to increase the precision of our measurement. We use a kinematic study of planetary nebulae in NGC 5128 (Peng, Ford, & Freeman 2004) which extends well into the galaxy halo. Peng, Ford, & Freeman (2004) report the rotation curve and velocity dispersion along the photometric major axis out to $80'$, including planetary nebulae within a perpendicular distance of $\pm 120''$ to this axis. The largest radii are not important to us as we are mainly interested in the

gravitational potential at smaller radii; we include their first three points only, extending our kinematic coverage to $2r_{eff}$. These kinematic data are rotation velocities and velocity dispersions, not full LOSVDs. In our dynamical modeling, we assume Gaussian LOSVDs with first and second moments to match the planetary nebulae data for these points. The lack of higher order information at these large radii does not effect the BH mass measurement. The planetary nebulae data are shown in figure 7 and presented in table 1.

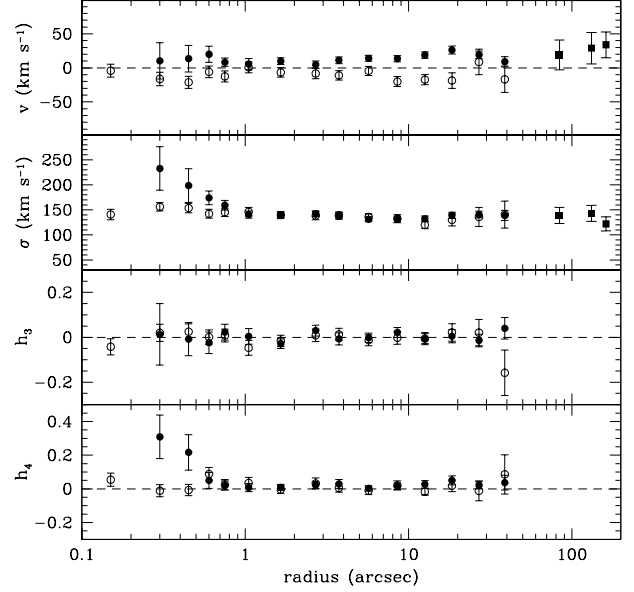


FIG. 7.— Gauss-Hermite moments of the LOSVDs along the slit perpendicular to the dust disk (filled circles) and along the slit parallel to the dust disk but offset from the center (open circles). The filled squares are from Peng, Ford, & Freeman (2004) and are along the same axis as the filled circles.

3. DYNAMICAL MODELS

The dynamical models are constructed as in Gebhardt et al. (2000c) and Gebhardt et al. (2003) using the orbit superposition technique first proposed by Schwarzschild (1979). We use the surface brightness profile described above to estimate the luminosity density distribution; the surface brightness can be deprojected assuming axisymmetry and some chosen inclination. This luminosity density then translates to a mass density distribution, assuming some stellar mass-to-light (M/L) ratio and BH mass. It is this mass density distribution which then defines the potential for a given model. Using this derived potential, we follow a representative set of orbits which sample the available phase space. We then determine the orbit superposition (i.e. nonnegative set of weights for the orbits) which provides the best match (the minimum χ^2) to the data. We can impose smoothness on the phase-space distribution function by maximizing entropy (Richstone & Tremaine 1988; Thomas et al. 2004). We repeat this process for a variety of BH masses, M/L ratios, and inclinations to find the overall best match.

To obtain a smooth χ^2 distribution, it is necessary to include an adequate number of orbits. We sample the gravitational potential by launching orbits from points in the three-dimensional space spanned by the energy E , the angular momentum L_z , and the third integral I_3 . The limits of this space are well-understood, and Richstone et al. (2004) details the

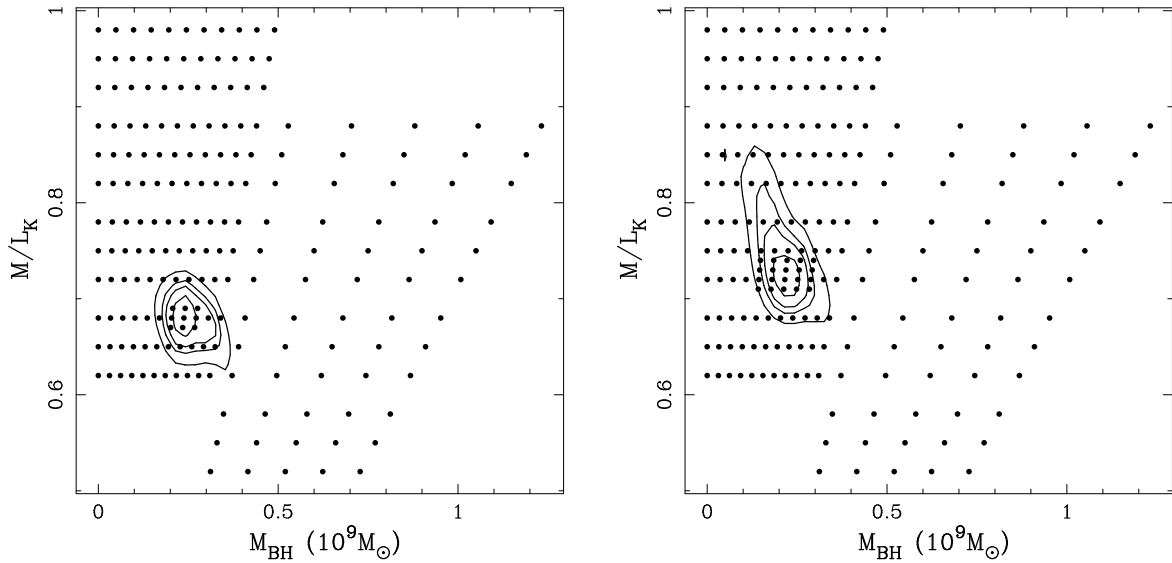


FIG. 8.— Two-dimensional plots of χ^2 as a function of BH mass and M/L ratio for both orientations we modeled. The left-hand panel shows models with rotation along the galaxy’s photometric major axis (PHOT models) and the right-hand panel shows models with rotation along the dust disk (DUST models). The points represent models. The contours were determined by a two-dimensional smoothing spline interpolated from these models and represent $\Delta\chi^2$ of 1.0, 2.71, 4.0, and 6.63 (corresponding to 68%, 90%, 95%, and 99% for 1 degree of freedom).

considerations for the sampling of this phase space. Our final model contains $\sim 10,000$ orbits, adequate to obtain a smooth χ^2 distribution for our binning scheme.

To compare the model with the data, we map both the observations and orbits to a grid of 20 radial bins, 5 angular bins, and 17 velocity bins. The time a given orbit spends in a given bin translates to its contribution to the light in that bin, and thus the mass. The radial binning scheme for the model is the same as that for the data shown in figure 7 and table 1; we have data on the major and minor axes, i.e. in two angular bins of the model. The binning schemes are chosen to maximize the S/N of the data. The velocity bins span the minimum and maximum velocities of the orbits; these must be chosen carefully because the high-velocity wings of the LOSVD are affected the most by a BH. We incorporate seeing in the model by convolving the light distribution for each orbit with the PSF of the kinematic observations. The Gemini observing runs had PSFs, approximated as Gaussians, of $0''.45$ in the March run and $0''.60$ in the June run. The planetary nebulae data have such large binning that seeing does not affect them.

For each model, we use the best-fit orbit superposition to match the light in each of the 100 spatial bins and the LOSVDs in the 33 bins where we have data. We fit to the full LOSVDs, not a parameterization such as the Gauss-Hermite moments. The orbit weights are chosen so that the luminosity density in each spatial bin matches the data to better than 1%, with typical matches better than 0.1%. This match is treated as a constraint, not as a difference to be minimized. We do minimize χ^2 for each model, with $\chi^2 = \sum [(y_i - y'_i) / \sigma_i]^2$, where the y_i ’s are the LOSVD bin heights of the data, the y'_i ’s are the LOSVD bin heights of the model, and σ_i is the uncertainty of the bin height of the data. Each combination of BH mass and stellar M/L ratio has an orbit superposition which

gives a minimum χ^2 ; we then compare the χ^2 of different such combinations to find the best match to the data. We use this measure of χ^2 to determine the uncertainties in the BH mass and stellar M/L as well. These are correlated, as the model can exchange mass in the BH for higher M/L , and thus we use the two-dimensional χ^2 distribution to determine the 68% confidence bands for these quantities, where $\Delta\chi^2 = 1$ for one degree of freedom.

4. RESULTS

The fact that NGC 5128 has rotation along more than one axis has interesting implications for its dynamical structure. This galaxy is either tumbling or triaxial. Tumbling is not an equilibrium dynamical state, but as a recent major merger, NGC 5128 may well not be in dynamical equilibrium. Strictly speaking, this means that we cannot match well the kinematics of NGC 5128 and the kinematics of an axisymmetric orbit superposition model. In our models, we choose to identify one axis of the observations with the rotation axis of the model; the rotation on the other axis serves only to balloon up the χ^2 . We find that the best-fitting models for NGC 5128 constructed in this way are not very good fits and have unrealistic characteristics; we choose to take another approach.

We return to our LOSVDs in each bin and symmetrize them about $v = 0$, taking the mean of each side to make the new, symmetric LOSVD. These new LOSVDs have no net rotation. This is not the true state of NGC 5128, but the resulting LOSVDs do imply approximately the same enclosed mass as our “true” LOSVDs. The kinetic energy is proportional to $(v^2 + \sigma^2)$; using a symmetric LOSVD forces the kinetic energy into the σ^2 term. We can then build orbit superposition models to match the “true” kinematics along one axis which we identify as the axis of rotation and these no-rotation kinematics along the other axis.

We are then faced with the quandary of which axis to identify as the rotation axis. It seems logical that the rotation along the direction of the dust disk at small radii would be important for the determination of the BH mass; however, inclusion of rotation at large radii also has important effects on inferred BH masses (Richstone et al. 2004). It is unclear what the best choice would be, especially since BH masses have not been determined using orbit superposition models for galaxies with such complex dynamical structure as NGC 5128. We thus choose to repeat our entire modeling procedure for both cases, first matching to the rotating kinematics along the dust disk axis and non-rotating kinematics along the photometric major axis (hereafter DUST), then switching to rotating kinematics along the photometric major axis and non-rotating kinematics along the dust disk axis (hereafter PHOT). We can thus compare the BH masses inferred by including different data.

Figure 8 presents the results of this process. Each panel shows χ^2 as a function of BH mass and M/L ratio, obtained by comparing model kinematics to observed kinematic data for NGC 5128. The left panel shows the DUST models and the right panel shows the PHOT models. The contours are drawn using a two-dimensional smoothing spline (Wahba 1990) but the modeled values are fairly smooth and large smoothing is not necessary. Figure 9 presents the χ^2 goodness of fit as a function of black hole mass; we have marginalized the two-dimensional χ^2 distributions shown in figure 8 over M/L to obtain these distributions. The dashed line and open squares are for the DUST models while the solid line and filled circles are for the PHOT models. The points show the χ^2 of individual models; the lines are marginalized from the smoothed distributions illustrated in the contours shown in figure 8. The models with rotation along the dust axis had overall higher χ^2 values so these are offset vertically for plotting purposes.

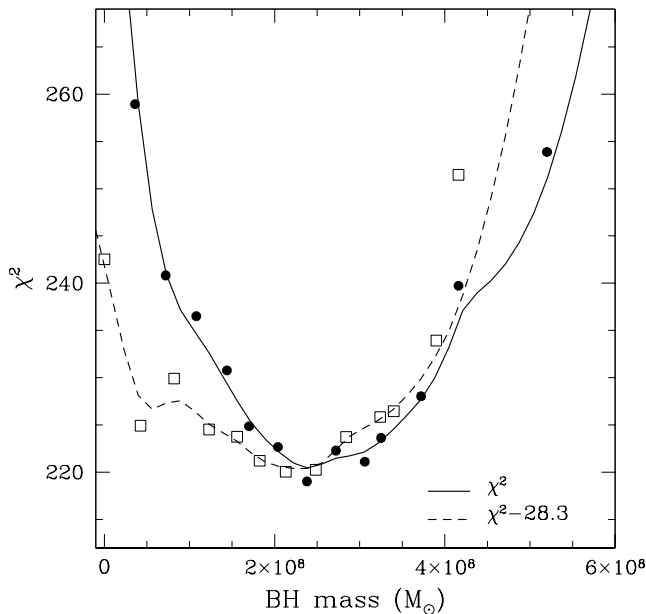


FIG. 9.— The χ^2 goodness of fit obtained by comparing model kinematics to observed kinematic data for NGC 5128, versus model black hole mass. The dashed line and open squares are for the models with the rotation axis along the dust disk (DUST models), and the solid line and filled circles are for the models with the rotation axis along the photometric major axis of the galaxy (PHOT models).

The BH masses from the two sets of models are in excellent agreement. For the PHOT models, the BH mass is $2.4^{+0.3}_{-0.2} \times 10^8 M_\odot$; for the DUST models, it is $2.2^{+0.3}_{-0.3} \times 10^8 M_\odot$. The PHOT models have significantly lower χ^2 ($\Delta\chi^2 = 28.3$), so we identify this as the preferred orientation. The photometric major axis of the galaxy (the rotation axis of the PHOT models) is the important axis for most of the galaxy's mass; it is reasonable that this is more important for a dynamical model of the galaxy. The M/L_K ratios are $0.68^{+0.01}_{-0.02}$ for the PHOT models and $0.72^{+0.03}_{-0.02}$ for the DUST models. These are not in agreement to within the 68% confidence limits but are close. Interestingly, there is some covariance in the DUST models but very little in the PHOT models. The PHOT models use the data that were well-centered on the galaxy nucleus on the model's rotation axis. In contrast, the DUST models use the data that were offset from the nucleus along the direction of the model's rotation axis and thus do not have any data on the actual rotation axis of the model. Such data appear to be important in breaking the degeneracy between BH mass and M/L ratio and placing the strongest constraints on each quantity.

Figure 10 compares the model kinematics with the observed kinematics for each axis on which we have data, for each orientation of rotation that we modeled. The left panels are for the PHOT models and the right panels are for the DUST models. The squares are from the photometric major axis and the circles are from the axis parallel to the dust disk but offset from the nucleus. The open symbols are the actual (or symmetrized) data and the filled or starred symbols are from the models. We emphasize that we fit the full LOSVDs and that this plot shows only the Gauss-Hermite moments of the LOSVDs. Notice the symmetrization of the observed data; $v = 0$ for every radial point on the dust axis for the PHOT models and every radial point on the photometric major axis for the DUST models.

NGC 5128 appears very round but it is possible that it is intrinsically quite flattened. Dynamical models such as those of Wilkinson, Sharples, Fosbury, & Wallace (1986) and Hui, Ford, Freeman, & Dopita (1995) conclude that is indeed flattened, with axis ratios of 1:0.98:0.55 and 1:0.92:0.79. The orbit-based models described above are all for an edge-on configuration, i.e. assuming that NGC 5128 is indeed nearly intrinsically round. We test the effect of using a model with different inclinations. We take the case of inclination $i = 20^\circ$, which implies axis ratios of 1:1:0.5, and $i = 45^\circ$, which implies axis ratios of 1:1:0.9. Figure 11 presents the results for the PHOT configuration of the kinematic data, the two-dimensional distribution of χ^2 as a function of BH mass and M/L ratio. The best-fit BH mass for $i = 20^\circ$ is $1.5^{+0.3}_{-0.2} \times 10^8 M_\odot$ and the best-fit M/L_K ratio is $0.68^{+0.02}_{-0.02}$. The M/L_K ratio is in good agreement with the edge-on models but the BH mass is $\sim 30\%$ smaller. Previous studies using this technique (Gebhardt et al. 2000c, 2003) have found that on average, inclination appears to cause a 30% random change in the BH mass, exactly what we find here. The best-fit BH mass for $i = 45^\circ$ is $1.8^{+0.4}_{-0.4} \times 10^8 M_\odot$ and the best-fit M/L_K ratio is $0.53^{+0.04}_{-0.03}$, a BH mass intermediate between the other two inclinations. The edge-on and $i = 20^\circ$ estimates of the BH mass are only different by 2σ and this somewhat smaller BH mass does not markedly affect our conclusions below. The χ^2 of the edge-on model is significantly less than either inclined model ($\Delta\chi^2 \sim 100$) so we adopt that value for the BH mass.

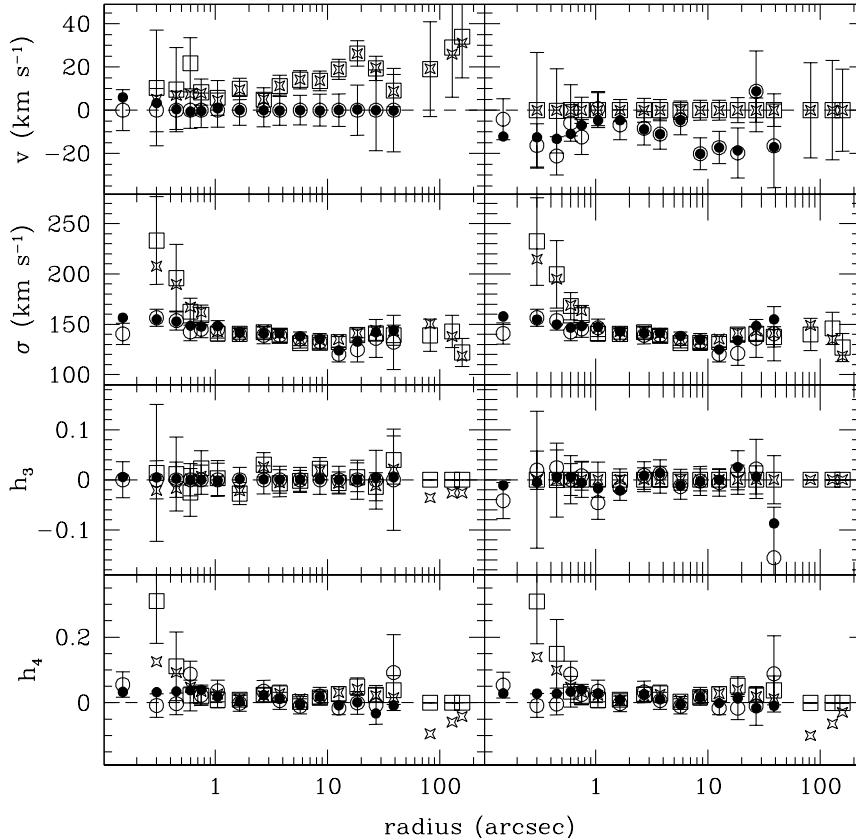


FIG. 10.— Comparison of observed kinematic data along each slit for NGC 5128 with model kinematics for the two best-fitting edge-on models. The left-hand panel compares to the best-fitting edge-on model with rotation along the photometric major axis (PHOT models) and the right-hand panel compares to the best-fitting edge-on model with rotation along the dust disk (DUST models). The open symbols are the data: circles for the axis parallel to the dust disk but offset from the center and squares for the galaxy photometric major axis. The filled circles are from the model on the axis parallel to the dust disk and the starred squares are from the model on the galaxy photometric major axis.

5. DISCUSSION

Our BH masses for all modeled inclinations are in good agreement with the gas dynamical results of Marconi et al. (2001). This agreement supports these authors' claim that the gas kinematics of NGC 5128 are well described by an ordered gas disk and suggests that in such situations, gas dynamics give reliable estimates for BH masses. Also, NGC 5128 has the largest offset from the BH- σ correlation ever measured. The BH of NGC 5128 is five to ten times larger than it should be as predicted by this correlation. Marconi & Hunt (2003) use the BH mass from Marconi et al. (2001) to place NGC 5128 (along with ~ 25 other objects) in the correlation between BH mass and near-infrared bulge luminosity. Marconi & Hunt (2003) find that the spread in this correlation is similar to that of the BH- σ correlation. NGC 5128 does lie above this relation (i.e. its BH mass is somewhat high compared to its near-IR bulge luminosity) but it is not a striking outlier in this relation. Apparently, the history of NGC 5128 has caused it to have a very large BH mass for its velocity dispersion but not an equally high BH mass compared to its near-IR bulge luminosity.

The remarkably high BH mass for NGC 5128 suggests that its BH assembled before the host stellar bulge. There are a few other observations that suggest this. Walter et al. (2004) use molecular gas observations of the host galaxy of a $z = 6.42$

quasar to show that it is missing the large stellar bulge implied by the BH- σ and BH- L_{bulge} correlations. A large BH is in place, but there does not appear to be an associated stellar bulge. This, along with our result for NGC 5128, is in sharp difference to the census of BHs in local galaxies described by Ho (2004) and others and the result for QSOs (Shields et al. 2003). There are several attractive theoretical models which explain the observed BH- σ correlation (Silk & Rees 1998; Fabian 1999; King 2003) and some also naturally explain such galaxy properties as color bimodality and the Faber-Jackson relation (Murray, Quataert, & Thompson 2004; Springel, Di Matteo, & Hernquist 2004). These models all use similar feedback arguments to show how an actively accreting BH can regulate its own growth by expelling gas from its immediate vicinity through an outflow or wind. The wind becomes stronger as the BH grows, driving away the gas that fuels the BH growth; the models connect the ultimate size the BH can attain with the host galaxy characteristics (i.e. σ). These models have been invoked to explain the BH- σ correlation of normal galaxies; understanding NGC 5128 and its offset from the BH- σ relation in the context of these arguments will provide an important clue for our understanding of the role of central BHs in galaxy formation.

Why is NGC 5128 such an unusual galaxy in this respect? The two most obvious possibilities are the recent ma-

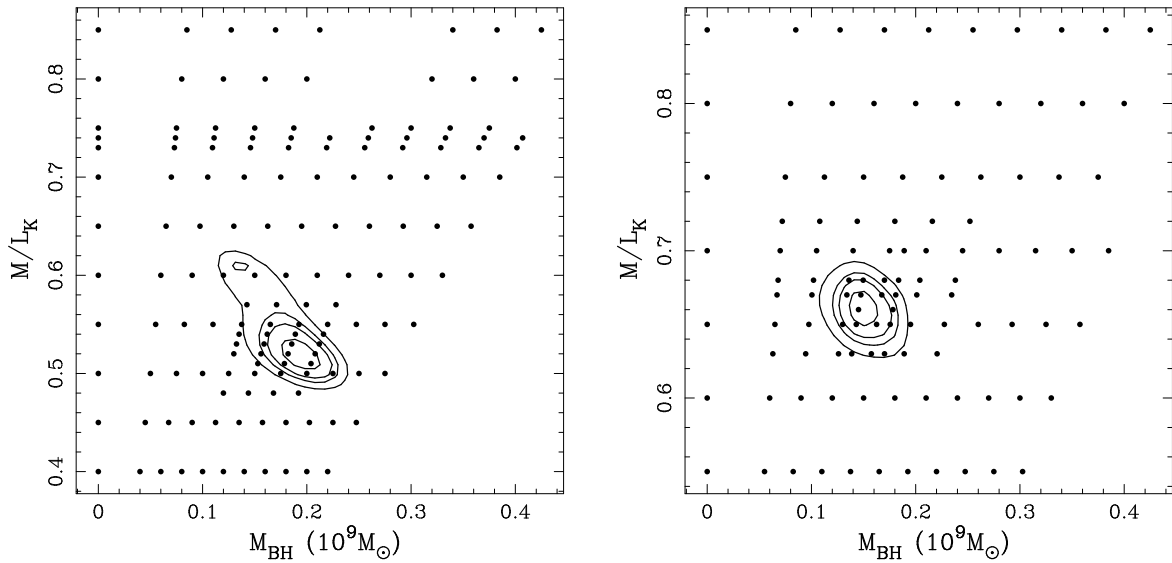


FIG. 11.— Same as figure 8 but for models with PHOT configuration and with inclination of 45° (left-hand panel) and 20° (right-hand panel).

major merger it has undergone and its AGN activity. The AGN activity seems to be a likely culprit. It is possible that a supermassive black hole that is currently growing by accreting material could be large compared to its host galaxy; perhaps the host galaxy has not had time to catch up to the growth of the BH. However, there has been some study of the BH- σ correlation in galaxies with active nuclei and this is not what has been found. Gebhardt et al. (2000b) studied the relationship between galaxy velocity dispersion and BH mass measured by reverberation mapping for a sample of active galaxies and found that these active galaxies are consistent with the BH- σ correlation for quiescent galaxies. Previously it had been noted that BH masses measured by reverberation mapping in active galaxies fall significantly below the correlation between bulge luminosity and BH mass determined from spatially resolved kinematics of nearby normal galaxies. This is interesting in light of our results for NGC 5128. Our BH mass for NGC 5128 is relatively consistent with the BH- L_{bulge} relationship but too high for the BH- σ correlation, while the reverberation mapping BH masses for AGN galaxies were too low for the BH- L_{bulge} correlation but consistent with the BH- σ correlation. Perhaps the reverberation mapping masses underestimate the true BH mass and AGN galaxies have larger BH masses for their velocity dispersions than quiescent galaxies. We need more BH masses measured through stellar (or possibly in some cases, gas) dynamics for active galaxies to further explore this issue.

NGC 5128's merger history presents another possibility which has been less studied until now. Perhaps some aspect of the merging process builds up the central black hole of a galaxy before later evolution causes the galaxy's velocity dispersion to catch up. For instance, if two galaxies with central supermassive BHs merge, their BHs may merge into one BH quickly while it may take much longer for the new galaxy to assume its final dynamical configuration. If some scenario like this is the case, we have happened to catch NGC 5128

at this stage in its merger when its supermassive BH has this specific relationship to the galaxy as a whole. Little is known about the central BHs of galaxies that have undergone recent mergers; NGC 5128 is the first such galaxy to have its central BH measured.

It is also possible that both of these aspects are acting in NGC 5128, of course. For both of these questions, using near-infrared kinematics holds promise for making progress. Many AGN and all recent merger galaxies are significantly dusty and thus inaccessible to optical spectroscopy. Using the techniques described here, we can reliably measure the kinematics of such galaxies. NGC 5128 is so enshrouded in dust that even its K -band light shows signs of reddening but this does not hamper our kinematic measurements or dynamical modeling. Also, with the untimely death of STIS on HST, our main method of measuring black holes has been eliminated and we can no longer rely on our previous techniques. If we want to continue to explore the connections between black holes and their host galaxies that HST first uncovered, the only method currently available is to use stellar kinematics measured at near-IR wavelengths. The excellent atmospheric seeing in the near-IR at good telescope sites, such as with Gemini and GNIRS, allows us to probe the central regions of nearby galaxies where the gravitational effects of the black hole are strongest. Also, as adaptive optics instrumentation becomes more available, we can push to higher spatial resolution and thus the sphere of influence of black holes of more distant galaxies.

We thank Bernadette Rodgers for assistance in understanding and using the GNIRS instrument during the system verification process. KG and JS gratefully acknowledge the support of the Texas Advanced Research Program and Grant No. 003658-0243-2001. KG acknowledges NSF CAREER grant AST-0349095. This publication is based on observations obtained at the Gemini Observatory, which is operated by the

Association of Universities for Research in Astronomy, Inc., under a cooperative agreement with the NSF on behalf of the Gemini partnership: the National Science Foundation (United States), the Particle Physics and Astronomy Research Council (United Kingdom), the National Research Council (Canada), CONICYT (Chile), the Australian Research Council (Australia), CNPq (Brazil) and CONICET (Argentina). This pub-

lication makes use of data products from the Two Micron All Sky Survey, which is a joint project of the University of Massachusetts and the Infrared Processing and Analysis Center/California Institute of Technology, funded by the National Aeronautics and Space Administration and the National Science Foundation.

REFERENCES

- Baade, W. & Minkowski, R. 1954, *ApJ*, 119, 215
 Beers, T. C., Flynn, K., & Gebhardt, K. 1990, *AJ*, 100, 32
 Cappellari, M. 2002, *MNRAS*, 333, 400
 Fabian, A. C. 1999, *MNRAS*, 308, L39
 Ferrarese, L. & Merritt, D. 2000, *ApJ*, 539, L9
 Gaffney, N., Lester, D., & Doppmann, G. 1995, *PASP*, 107, 68
 Gebhardt, K., et al. 2000, *ApJ*, 539, L13
 Gebhardt, K., et al. 2000, *AJ*, 119, 1157
 Gebhardt, K., et al. 2003, *ApJ*, 583, 92
 Haehnelt, M. G. & Kauffmann, G. 2000, *MNRAS*, 318, L35
 Hui, X., Ford, H. C., Freeman, K. C., & Dopita, M. A. 1995, *ApJ*, 449, 592
 Israel, F. P. 1998, *A&A Rev.*, 8, 237
 Ho, L. C. W. 2004, *Coevolution of Black Holes and Galaxies*, 293
 Jarrett, T. H., Chester, T., Cutri, R., Schneider, S. E., & Huchra, J. P. 2003, *AJ*, 125, 525
 King, A. 2003, *ApJ*, 596, L27
 Lester, D., & Gaffney, N. 1994, *ApJ*, 431, L13
 Malin, D. F., Quinn, P. J., & Graham, J. A. 1983, *ApJ*, 272, L5
 Marconi, A., Schreier, E. J., Koekemoer, A., Capetti, A., Axon, D., Macchetto, D., & Caon, N. 2000, *ApJ*, 528, 276
 Marconi, A., Capetti, A., Axon, D. J., Koekemoer, A., Macchetto, D., & Schreier, E. J. 2001, *ApJ*, 549, 915
 Marconi, A. & Hunt, L. K. 2003, *ApJ*, 589, L21
 Murray, N., Quataert, E., & Thompson, T. A. 2004, *astro-ph/0406070*
 Ostriker, J. P. 2000, *Physical Review Letters*, 84, 5258
 Peng, E. W., Ford, H. C., & Freeman, K. C. 2004, *ApJ*, 602, 685
 Quillen, A. C., Graham, J. R., & Frogel, J. A. 1993, *ApJ*, 412, 550
 Rejkuba, M. 2004, *A&A*, 413, 903
 Richstone, D. O. & Tremaine, S. 1988, *ApJ*, 327, 82
 Richstone, D., et al. 2004, *astro-ph/0403257*
 Schreier, E. J., et al. 1998, *ApJ*, 499, L143
 Schwarzschild, M. 1979, *ApJ*, 232, 236
 Sarzi, M., et al. 2002, *ApJ*, 567, 237
 Shields, G. A., Gebhardt, K., Salviander, S., Wills, B. J., Xie, B., Brotherton, M. S., Yuan, J., & Dietrich, M. 2003, *ApJ*, 583, 124
 Silge, J. D. & Gebhardt, K. 2003, *AJ*, 125, 2809
 Silk, J. & Rees, M. J. 1998, *A&A*, 331, L1
 Springer, V., Di Matteo, T., & Hernquist, L. 2004, *astro-ph/0411108*
 Thomas, J., Saglia, R. P., Bender, R., Thomas, D., Gebhardt, K., Magorrian, J., & Richstone, D. 2004, *MNRAS*, 353, 391
 Tonry, J., Dressler, A., Blakeslee, J., Ajhar, E., Fletcher, A., Luppino, G., Metzger, M., & Moore, C. 2001, *ApJ*, 546, 681
 Wahba, G. 1990, *Spline Models for Observational Data* (Philadelphia: SIAM)
 Wallace, L., & Hinkle, K. 1997, *ApJS*, 111, 445
 Walter, F., Carilli, C., Bertoldi, F., Menten, K., Cox, P., Lo, K. Y., Fan, X., & Strauss, M. A. 2004, *ApJ*, 615, L17
 Wilkinson, A., Sharples, R. M., Fosbury, R. A. E., & Wallace, P. T. 1986, *MNRAS*, 218, 297

TABLE 1
GAUSS-HERMITE MOMENTS OF LOSVDs FOR NGC 5128

radius ($''$)	parallel to dust disk, offset				perpendicular to dust disk, centered			
	v (km s^{-1})	σ (km s^{-1})	h_3	h_4	v (km s^{-1})	σ (km s^{-1})	h_3	h_4
0.00	-12±10	153±13	0.036±0.053	0.056±0.051				
0.15	-4±9	141±11	-0.042±0.036	0.054±0.039				
0.30	-16±10	156±9	0.020±0.038	-0.011±0.036	10±27	233±44	0.013±0.137	0.309±0.129
0.45	-21±9	154±9	0.025±0.035	-0.007±0.033	14±19	198±34	-0.008±0.074	0.217±0.105
0.60	-6±8	142±9	0.001±0.032	0.088±0.039	20±12	174±14	-0.024±0.048	0.050±0.047
0.75	-12±8	145±8	0.008±0.029	0.025±0.031	8±6	159±10	0.023±0.035	0.020±0.027
1.05	1±8	146±9	-0.047±0.033	0.035±0.033	6±8	141±7	0.004±0.035	0.008±0.024
1.65	-7±7	140±7	-0.016±0.025	-0.004±0.024	10±5	140±5	-0.028±0.022	0.009±0.018
2.70	-8±8	139±8	0.009±0.028	0.032±0.033	5±5	142±6	0.030±0.024	0.024±0.021
3.75	-11±7	139±7	0.013±0.027	0.006±0.026	11±5	138±6	-0.007±0.027	0.029±0.026
5.70	-4±7	136±7	-0.013±0.025	-0.011±0.023	14±4	131±5	-0.002±0.021	0.003±0.016
8.55	-20±7	133±8	-0.002±0.029	0.020±0.027	14±5	132±5	0.022±0.022	0.016±0.019
12.60	-17±7	120±7	-0.006±0.027	-0.017±0.020	19±5	132±5	-0.006±0.022	0.027±0.022
18.45	-19±12	130±12	0.022±0.039	0.018±0.035	26±6	139±6	0.005±0.029	0.050±0.027
27.00	9±19	136±19	0.021±0.059	-0.012±0.059	19±6	141±7	-0.014±0.028	0.022±0.021
38.85	-17±19	141±27	-0.158±0.101	0.086±0.116	9±8	139±10	0.040±0.048	0.037±0.044
82.35					19±22 ^a	139±16 ^a		
129.4					29±23 ^a	143±16 ^a		
158.8					34±19 ^a	122±14 ^a		

REFERENCES. — (a) Peng, Ford, & Freeman (2004)